

# Prediction of creep crack initiation behaviour in 316H stainless steel using stress dependent creep ductility

Hanna Quintero, Ali Mehmanparast\*

Offshore Renewable Energy Centre, Cranfield Energy, Cranfield University, Bedfordshire,  
MK43 0AL

---

## A B S T R A C T

---

---

*Keywords:*

Creep crack initiation

Constraint effects

Creep ductility

Specimen geometry

316H stainless steel

Long term

Transition

The creep crack initiation behaviour of Type 316H stainless steel at 550 °C has been predicted by implementing a stress dependent creep ductility and average creep strain rate model in finite element analyses. Simulations were performed on five specimen geometries: C(T), CS(T), DEN(T), M(T) and SEN(T). The predicted results have been characterised using the  $C^*$  fracture mechanics parameter and the short-term, long-term and transition creep crack initiation trends are predicted for each of the specimen geometries examined. The prediction results have been validated through comparison with experimental data available in the literature. The predicted short-term and long-term creep crack initiation trends have also been compared with NSW prediction lines. The predicted results, from each specimen geometry, are compared to each other and the differences in crack initiation trends have been discussed in terms of the specimen geometry, in-plane constraint and stress level effects on the creep crack initiation behaviour of the material. A mesh sensitivity analysis has also been performed to find the optimum mesh size for performing crack initiation simulations.

---

\*Corresponding author. Tel +44 1234 75 8331

E-mail address: a.mehmanparast@cranfield.ac.uk

# 1 Introduction

It is known that Creep Crack Growth (CCG) is the main failure mechanism in many of the engineering components operating at elevated temperatures. In order to assess the structural integrity of these high temperature components, it is necessary to characterise the creep properties of the material in order to predict the creep crack initiation (CCI) and growth behaviour of the components. Type 316H stainless steel (SS) is widely used in the UK power plant components, with an operating temperature of around 550 °C. Significant research has previously been done to characterise the CCI and CCG behaviour of this material at high temperatures to provide reliable remaining life estimates for the components made of this material. Although CCG has been the main focus of most of the experimental testing programmes, the period of time required to initiate a crack from a pre-existing defect introduced in fracture mechanics specimens may take up to 80% of the test duration [1]. Therefore, in component life assessments, it is essential to predict the CCI behaviour of the material. The onset of crack growth from a pre-existing defect is often denoted incubation time and in this paper is referred to as creep crack initiation time.

A large number of experimental and numerical CCI and CCG investigations have previously been carried out on a range of fracture specimen geometries made of 316H SS to determine the long-term and short-term behaviour of the material [2]–[9]. In the majority of the existing analytical and numerical CCG prediction models, the uniaxial creep ductility (i.e. creep strain at failure) and uniaxial creep properties have been assumed constant and unchanged in short-term and long-term tests. Thus, accelerated high load (i.e. short-term) CCG predictions have been extrapolated to predict the long-term behaviour of the material. However, it has been noted that short-term (i.e. high load) tests can influence the plastic zone size ahead of the crack tip, due to the relatively low yield stress of the material ( $\sigma_{0.2} = 170$  MPa at 550 °C), which can cause reduction in the specimen constraint level and subsequently lower CCG rates [9]–[11]. An experimental investigation of the CCG behaviour in 316H at 550 °C in [11] has confirmed that due to the change in the specimen constraint level under different loads, a different CCG trend was observed in long-term tests compared to the short-term experimental data.

<b>Nomenclature</b>			
		$t_i$	Creep crack initiation time
$a$	Crack length	$t_r$	Creep rupture time
$a_0$	Initial crack length	$v_r$	Creep rupture stress exponent
$\dot{a}$	Creep crack growth rate	$W$	Specimen width
$\dot{a}_0$	Initial creep crack growth rate	$\dot{\Delta}$	Load line displacement rate
$\dot{a}_{NSW}$	Creep crack growth rate predicted by NSW model	$\epsilon_f$	Uniaxial creep ductility
$\Delta a$	Crack extension	$\epsilon_f^*$	Multiaxial creep ductility
$A$	Power law stress coefficient	$\dot{\epsilon}_s$	Steady state creep strain rate
$A_A$	Average power law stress coefficient	$\dot{\epsilon}_A$	Average creep strain rate
$B$	Specimen thickness	$\dot{\epsilon}_c$	Equivalent creep strain rate
$B_n$	Specimen net thickness	$\eta$	Non dimensional function of specimen geometry
$B_r$	Temperature dependent rupture constant	$\theta$	Crack tip angle
$C^*$	Steady state creep fracture mechanics parameter	$\sigma$	Applied stress
$D$	Material constant coefficient in correlation of creep crack growth rate with $C^*$	$\sigma_{0.2}$	0.2% proof stress
$E$	Young's modulus	$\sigma_e$	Equivalent stress
$H$	Non-dimensional function of specimen geometry and $n$	$\sigma_m$	Mean stress
$I_n$	Non-dimensional function of $n$	$\sigma_{ref}$	Reference stress
$K$	Stress intensity factor	$\sigma_y$	Yield stress of the material
$L$	Specimen half-length	$\phi$	Material constant exponent in correlation of creep crack growth rate with $C^*$
$MSF$	Multiaxial strain factor	$\theta_i$	Creep crack initiation angle
$n$	Power law creep stress exponent	$\omega$	Creep damage parameter
$n_A$	Average power law creep stress exponent	$\dot{\omega}$	Creep damage rate
$P$	Applied load	CCG	Creep Crack Growth
$P_{LC}$	Plastic collapse load	CCI	Creep Crack Initiation
$r_c$	Creep process zone	NSW	Nikbin, Smith and Webster creep crack growth model
$R_i$	C shaped cracked specimen inner radius	NSW-MOD	Modified version of Nikbin, Smith and Webster creep crack growth model
$R_o$	C shaped cracked specimen outer radius		
$t$	Time	FE	Finite Element
$t_{0.2}$	Time for 0.2mm crack extension	PE	Plane strain
$t_{0.5}$	Time for 0.5mm crack extension	PS	Plane stress

A study was recently conducted to show that the uniaxial creep properties in 316H SS are different from short-term to long-term tests, resulting in a new approach to estimate creep ductility trends that are dependent on the applied stress normalised by the yield stress, thus accounting for the plasticity effects on the creep behaviour of the material [12]. The result of this work implies that the use of short-term data to predict long-term behaviour is inappropriate, due to the observed difference in short-term and long-term creep tests. Since components are usually subjected to relatively low load levels compared with those applied in accelerated short-term tests, the new estimated trends presented in [12] provide a more accurate approach for the analysis and design of high temperature components operating at low stresses. The stress dependent creep ductility trends developed in [12] were implemented in finite element (FE) simulations to predict

the CCG behaviour in compact tension, C(T), 316H specimens, and good agreements were found between FE predictions and experimental data [12],[13].

It is evident in the literature that the focus of CCG experimental testing programmes has mainly been on standard C(T) specimen geometry since it provides conservative CCI and CCG trends due to the high constraint level. However, the ASTM standard [14] and European CoP [10] recommend, within the possibilities, performing tests on different fracture specimen geometries, specimen size and dimensions, in order to increase the confidence in the material crack growth data produced. The characterisation of the CCI and CCG behaviour in other specimen geometries allows the data to be used in defect tolerance assessment of components [10] as well as more realistic and reasonable predictions for components that are compatible with lower constraint specimens. According to the ASTM standard [14] and the European CoP [10], additional industrial-relevant geometries valid for CCI and CCG testing are C-shaped cracked specimen in tension, CS(T), double edge notched specimen in tension, DEN(T), middle cracked specimen in tension, M(T) and single edge notched specimen in tension, SEN(T).

Loading conditions, crack length, specimen size and geometry affect the state of stress at the crack tip, which can subsequently influence the CCI and CCG behaviour of the material [14]–[20]. It has been observed that CCG rates in steel generally increase with specimen thickness [15] and decrease with a reduction in the constraint level [16], while recent studies have found that the creep behaviour is also stress regime dependent [12], [19]–[22]. Furthermore, the effects of fracture mechanics specimen geometry on the crack tip constraint level and subsequently crack growth behaviour of the material have been numerically investigated in [17] and experimentally observed in [23]–[27]. The findings show that CCG rates in the C(T) specimen are about five times higher compared to the M(T) specimen, therefore determining that for a given thickness and loading condition the C(T) specimen geometry induces a higher constraint level compared to the M(T) geometry.

In recent work by Mehmanparast [22], the CCG behaviour of 316H stainless steel at 550 °C was predicted for a range of specimen geometries, using a stress dependent creep ductility model, and good agreement was found between the predicted trends and the experimental data. The new stress dependent uniaxial creep properties presented in

[12] and [22] have not yet been examined to predict the short-term and long-term CCI behaviour of 316H SS at 550 °C. Therefore, in this work the stress dependent creep ductility model has been implemented in FE simulations to predict the short-term and long-term CCI behaviour of 316H stainless steel at 550 °C over a wide range of load levels in five specimen geometries. The specimen geometries considered are C(T), CS(T), DEN(T), M(T) and SEN(T), in order to investigate the specimen geometry, therefore in-plane constraint, effects on the CCI behaviour of the material. The CCI trends obtained from FE simulations have been validated through comparison with experimental data available in the literature. Comparisons have also been made between the predicted results and the analytical creep crack initiation prediction model developed by Nikbin, Smith and Webster (NSW) [2].

## 2 Creep deformation and crack initiation

### 2.1 Uniaxial creep deformation

Uniaxial creep tests are performed on round bar specimens under a range of stresses to determine the creep properties of a material at a given temperature. The results from these tests are plotted in the form of creep strain versus time. The creep response of a material can be divided into three stages: primary, secondary and tertiary creep regions. The creep strain rate obtained from the secondary creep region is referred to as minimum or steady state creep strain rate,  $\dot{\epsilon}_s$ , and can be described, for a power law creeping material, by Norton's power law [1],[28]:

$$\dot{\epsilon}_s = A\sigma^n \quad (1)$$

where  $\sigma$  is the applied stress,  $A$  is the temperature dependent material constant and  $n$  is the power law creep stress exponent. Alternatively, the average creep strain rate,  $\dot{\epsilon}_A$ , which accounts for the three creep regions may be described as

$$\dot{\epsilon}_A = \frac{\epsilon_f}{t_r} \quad (2)$$

where  $\epsilon_f$  is the creep ductility and  $t_r$  is the creep rupture time. The stress dependency of the average creep strain rate can be described using the power law relationship

$$\dot{\epsilon}_A = A_A\sigma^{n_A} \quad (3)$$

where  $A_A$  and  $n_A$  are the average creep power law stress coefficient and exponent, respectively.

## 2.2 Stress dependency of uniaxial creep properties

The creep rupture time,  $t_r$ , at a given temperature under a range of stress levels can be described by the power law relationship

$$t_r = B_r \sigma^{-v_r} \quad (4)$$

where  $B_r$  is the temperature dependant rupture constant and  $v_r$  is the rupture life stress exponent. Using Eqns (2), (3) (4), the dependency of creep ductility on stress can be defined as

$$\varepsilon_f = A_A B_r \sigma^{n_A - v_r} \quad (5)$$

Eqn (5) shows that creep ductility becomes stress independent when  $n_A = v_r$ , otherwise, the creep ductility becomes a function of stress and is proportional or inversely proportional to a power of the applied stress when  $n_A > v_r$  or  $n_A < v_r$ , respectively.

It has been shown in [12] that the average creep strain rate and creep rupture behaviour for 316H SS at a given temperature may be represented by two power law fits to the low and high stress regions. Fig. 1 shows the stress dependent average creep strain rate and creep rupture trends for 316H SS at 550 °C, in which the applied stress has been normalised by 0.2% proof stress of the material.

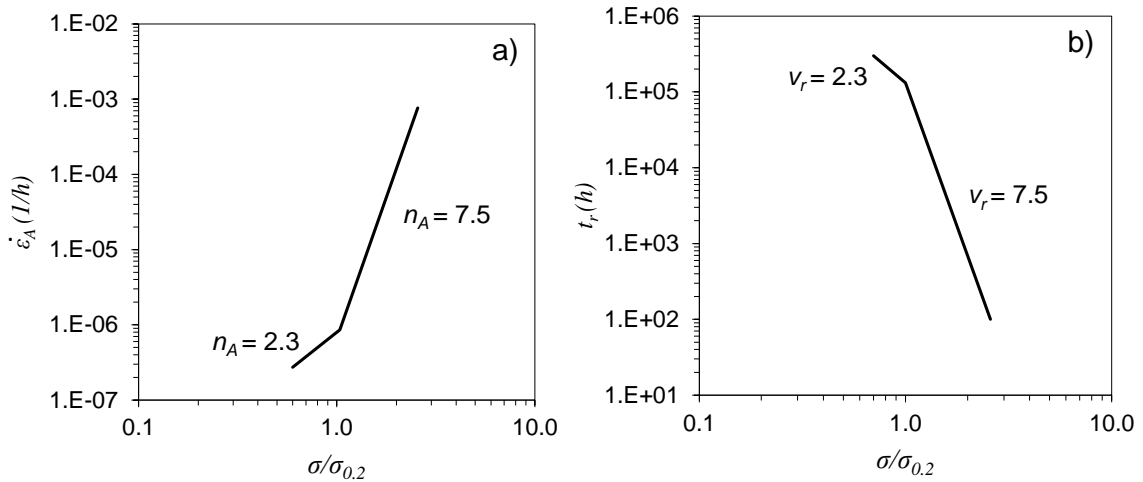


**Fig. 1.** (a) Average creep strain rate, (b) rupture time trends for 316H stainless steel at 550 °C [12]

From Fig. 1 and Eqn (5) it can be inferred that constant values of creep ductility are expected in the low and high normalised stress regions where  $n_A = v_r$ . However, at intermediate normalised stress levels ( $0.84 < \sigma/\sigma_{0.2} < 1.32$ ), the creep ductility becomes stress dependent. As seen in Fig. 2, the estimated creep ductility trends for 316H stainless steel at 550 °C consist of an upper shelf of 13.6% (for  $\sigma/\sigma_{0.2} \geq 1.32$ ), a lower shelf of 0.9% (for  $\sigma/\sigma_{0.2} \leq 0.84$ ) and a stress dependent transition region in between (for  $0.84 < \sigma/\sigma_{0.2} < 1.32$ ).

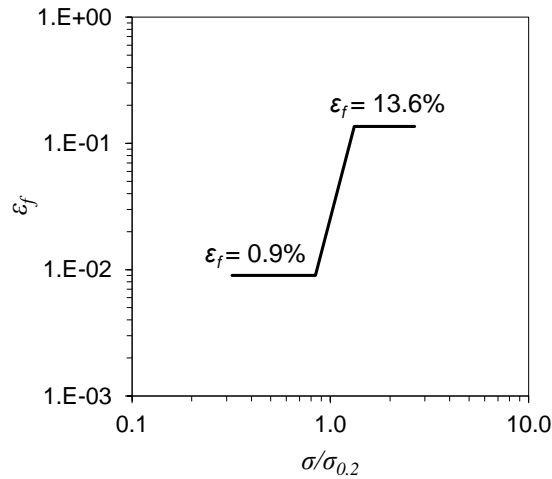


Fig. 2. Creep ductility trends for 316H stainless steel at 550 °C [12]

### 2.3 Creep crack initiation and growth

Creep crack initiation and growth tests are performed on fracture specimen geometries, which contain a pre-existing defect (i.e. starter crack). Prior to crack growth, a large amount of time is required for the creep damage to build up ahead of the crack tip. This period is often referred to as creep crack initiation time,  $t_i$ , and can be defined as the time for a small measurable crack extension to occur from a pre-existing defect, which is typically 0.2 mm or 0.5 mm and is denoted as  $t_{0.2}$  and  $t_{0.5}$ , respectively [14]. Over long periods, when a steady state of creep deformation and damage has developed ahead of the crack tip, the creep crack initiation time,  $t_i$ , may be correlated with the creep crack growth rate,  $\dot{a}$ , and alternatively characterised by the crack tip fracture mechanics parameter  $C^*$  using a power law relationship [1],[11]

$$t_i = \frac{\Delta a}{\dot{a}} = \frac{\Delta a}{DC^*\phi} \quad (6)$$

where  $D$  and  $\phi$  are CCG material constants and  $\Delta a$  is the small measurable crack extension. Under steady state conditions,  $\dot{a}$  vs.  $C^*$  data appear as a straight line on log-log axes; however, prior to this, the data points will appear as a “tail” region.

The  $C^*$  parameter can be calculated by

$$C^* = \frac{P\dot{\Delta}}{B_n(W-a)}H\eta \quad (7)$$

where  $P$  is the applied load,  $\dot{\Delta}$  is the creep load line displacement rate,  $B_n$  is the specimen net thickness,  $W$  is the width of the specimen and  $a$  is the crack length. In Eqn (7)  $H$  and  $\eta$  are non-dimensional geometry dependent parameters the solutions of which can be found in [14]. The ASTM E1457 standard [14] specifies the validity criteria in order to characterise the steady state creep crack growth behaviour of the material using the  $C^*$  parameter. The ASTM E1457 standard [14] also specifies the procedure to determine the creep load line displacement rate,  $\dot{\Delta}$ , which has been recommended to be taken as the total load line displacement rate in  $C^*$  calculations.

## 2.4 Normalised reference stress

The normalised reference stress provides a measure of the extent of plasticity ahead of the crack tip [1] and is defined by:

$$\frac{\sigma_{ref}}{\sigma_{0.2}} = \frac{P}{P_{LC}} \quad (8)$$

where  $P$  is the applied load,  $P_{LC}$  is the plastic collapse load in a cracked body for a perfectly-plastic material and  $\sigma_{0.2}$  is taken as the yield stress of the material. The solutions for  $P_{LC}$  in plane stress and plane strain conditions for various specimen geometries are given in [29]. If the normalised reference stress is much less than unity, the plasticity in the specimen is expected to be limited; however, if the normalised reference stress is much larger than unity, this indicates high plasticity, which can lead to a reduction in the specimen constraint level.

## 3 Creep crack initiation prediction models

In this work CCI has been predicted through analytical and FE simulations. Stress dependent creep properties have been employed in FE simulations and the results are

compared with analytical predictions from the NSW model in which constant creep properties are employed. The numerical and analytical CCI models are described next.

### 3.1 Finite element simulations

Creep crack initiation times have been predicted in different specimen geometries over a range of loading conditions using FE simulations. The FE models and creep damage calculations implemented in a subroutine are described below.

#### 3.1.1 Specimen geometries and mesh design

Two dimensional (2D) FE analyses have been conducted on five fracture mechanics specimen geometries with different in-plane constraint levels. The specimen dimensions considered in the FE analyses were chosen based on the dimensions of the samples tested in [11] and previous creep crack growth studies in [12], [22]. The dimensions are shown in Table 1 and the geometries in Fig. 3, where  $W$  is the specimen width,  $B$  is the specimen thickness,  $a_0$  is the initial crack length and  $L$  is the specimen half-length.

**Table 1.** Summary of specimen dimensions

Specimen geometry	Constraint level	$W$ (mm)	$B$ (mm)	$a_0/W$	$L$ (mm)	$R$ (mm)	
						$R_i$	$R_o$
C(T)	High	50	25	0.5	-	-	-
CS(T)	High	25	25	0.2	-	25	50
DEN(T)	Low	12.5	12.5	0.3	37.5	-	-
M(T)	Low	12.5	12.5	0.3	37.5	-	-
SEN(T)	Low	25	12.5	0.3	37.5	-	-

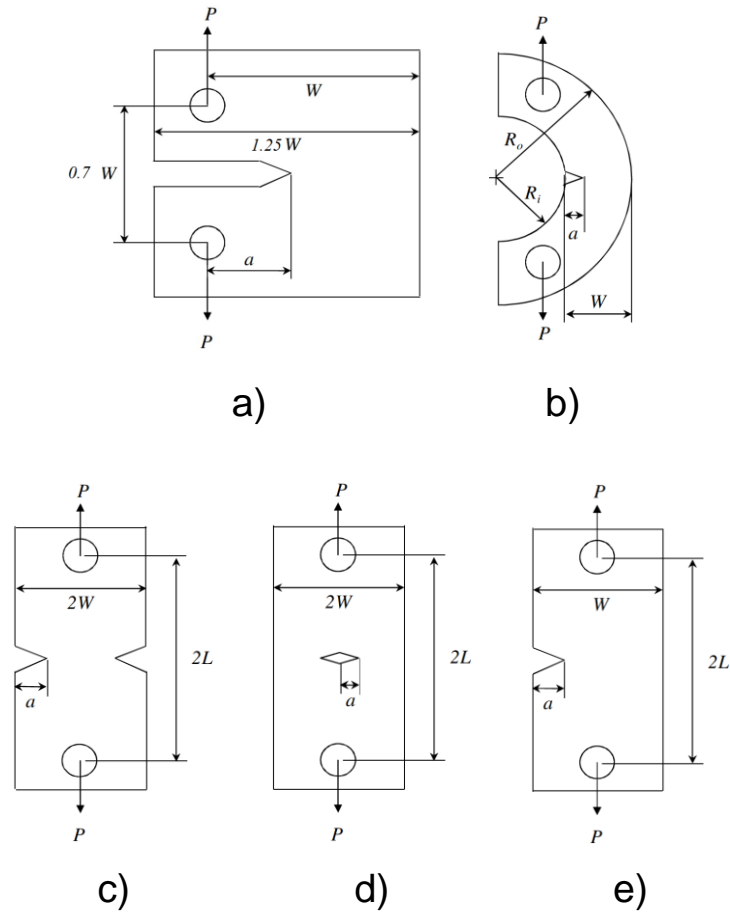


**Fig. 3.** Schematic illustration of specimen geometries (a) C(T), (b) CS(T), (c) DEN(T), (d) M(T), (e) SEN(T)

Symmetry boundary conditions were employed in the models, therefore only half of the geometry has been modelled for the C(T), CS(T) and SEN(T) specimens, while the DEN(T) and M(T) specimen models feature a quarter of the geometry. With regard to load application, for the C(T) and CS(T) specimen models the load has been applied to a reference point which represents the centre of the pin in the experimental tests. For the DEN(T), M(T) and SEN(T) specimen models, the total load has been uniformly distributed along the elements located at the top edge of the model, with a distance of  $L$  from the crack mouth opening plane. For the DEN(T), M(T) and SEN(T) specimen models, ends of the specimens were constrained to remain plane and not to rotate as the specimen deforms. The FE models and mesh designs for a range of fracture specimen geometries examined are shown in Fig. 4.

For all the models, a semi-circular focused mesh has been designed around the crack tip (see Fig. 4). A small geometry change analysis has been performed and the models have

been meshed using three-noded linear plane stress triangular elements (CPS3) in the first semi-circular ring at the crack tip, to introduce a sharp crack tip, and four-noded linear plane stress quadrilateral elements (CPS4) for the rest of the geometry. For the focused mesh, the element size spans from 10 to 500 $\mu\text{m}$ , for a distance of 5mm from the crack tip, biased towards the crack tip, as shown in Fig. 4. The optimum element size in the focused mesh region was chosen based on the mesh sensitivity analysis that is presented along with the prediction results in the next section. For each of the specimen geometries considered, a wide range of loads has been applied to cover a large range of  $C^*$  values. The loading conditions applied on each of the fracture specimen geometries examined in this study are summarised in Tables 3-7.

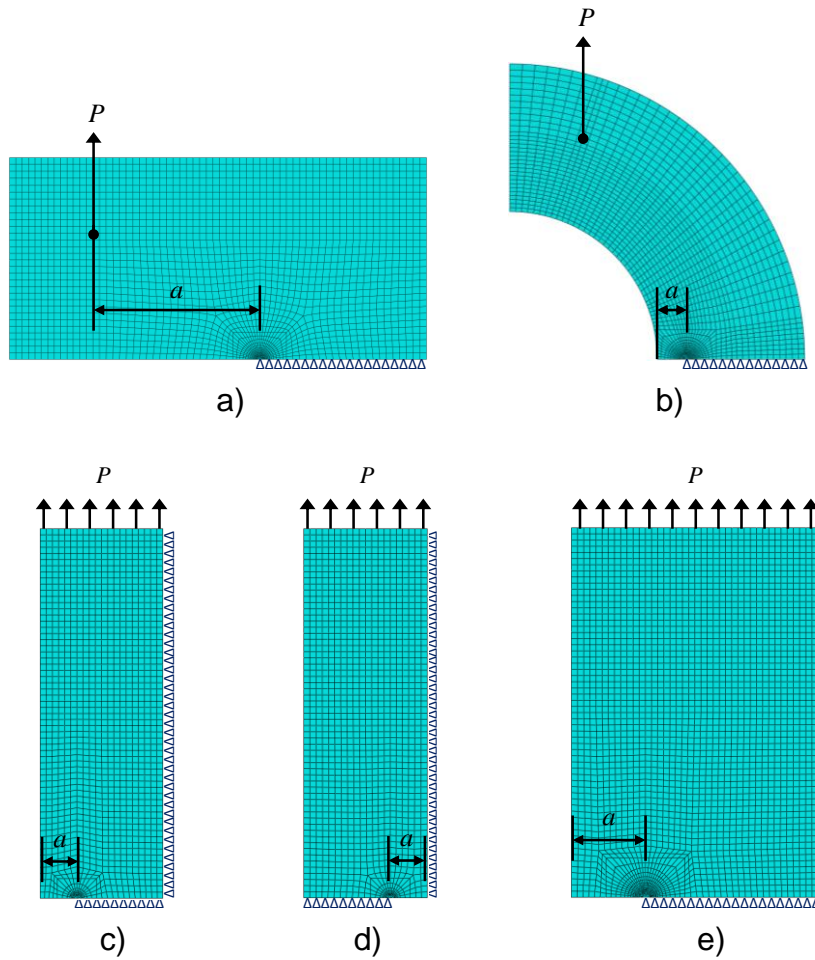


**Fig. 4.** Mesh design of specimen geometries (a) C(T), (b) CS(T), (c) DEN(T), (d) M(T), (e) SEN(T)

### 3.1.2 Elastic-plastic-creep properties

FE analyses have been performed using elastic-plastic-creep properties. The time independent elastic-plastic tensile data for the 316H stainless steel at 550 °C employed in FE simulations were taken from [30] and are shown in Fig. 5. As shown in this figure, to avoid numerical difficulties in FE simulations the high temperature tensile data have been smoothed by removing fluctuating data points, which occur at elevated temperatures due to dynamic strain aging effects. The Young's modulus  $E$  and yield stress  $\sigma_y$  (which is often taken as 0.2% proof stress,  $\sigma_{0.2}$ ) of the material at this temperature are 140 GPa and 170 MPa, respectively.

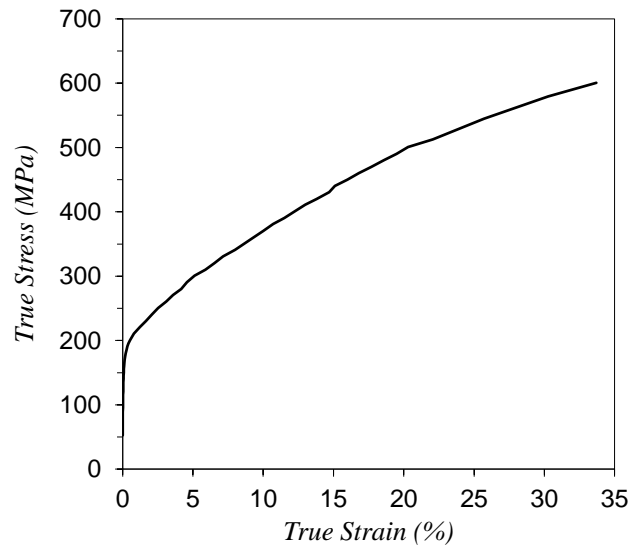


**Fig. 5.** Tensile curve for 316H stainless steel at 550 °C

The average creep strain rate (see Eqn (3)) has been defined in the model using stress dependent power law creep stress coefficients and exponents, as shown in Fig. 1. The average creep strain rate power law constants for the low stress ( $\sigma/\sigma_{0.2} < 1.035$ ) and high stress ( $\sigma/\sigma_{0.2} \geq 1.035$ ) regimes are listed in Table 2. Moreover, stress dependent creep ductility values of 0.9% at the lower shelf ( $\sigma/\sigma_{0.2} < 0.84$ ), 13.6% at the upper shelf ( $\sigma/\sigma_{0.2} > 1.32$ ) and a stress dependent transition region in between (see Fig. 2) have been employed in simulations.

**Table 2.** Average creep strain rate power law constants for 316H stainless steel at 550 °C

	$A_A$ (MPa <sup>-n</sup> h <sup>-1</sup> )	$n_A$
$\sigma/\sigma_{0.2} < 1.035$	$6.56 \times 10^{-12}$	2.3
$\sigma/\sigma_{0.2} \geq 1.035$	$1.24 \times 10^{-23}$	7.5

### 3.1.3 Creep crack initiation simulations

FE simulations were performed using ABAQUS 6.14 [31]. A user defined field (USDFLD) subroutine has been defined to calculate the creep damage at each time interval, in all elements, in ABAQUS simulations. The stress dependent creep ductility and average creep strain rate parameters shown in Fig. 1 and Fig. 2 are implemented in the subroutine such that at each time interval, appropriate values of  $A_A$ ,  $n_A$  and  $\varepsilon_f$  were determined in the subroutine based on the normalised stress level in each element. When an element is considered fully creep damaged, the crack growth is simulated by reducing the load carrying capacity of that element. This approach has been widely used in CCG and CCI simulations [3], [12], [13], [22], [32], [21], [33]. The creep damage model used in the FE simulations is described next and has been implemented in the subroutine.

The creep damage accumulation ahead of the crack tip has been modelled based on the creep ductility exhaustion approach, which has been widely used in the simulation of CCG and CCI [4], [7], [12], [22], [32], [21], [33], [34]. The accumulated creep damage parameter  $\omega$  is defined as

$$\omega = \int_0^t \dot{\omega} dt \quad (9)$$

where  $\dot{\omega}$  is the rate of damage accumulation, which can be expressed as

$$\dot{\omega} = \frac{\dot{\varepsilon}_c}{\varepsilon_f^*} \quad (10)$$

In Eqn (10)  $\dot{\varepsilon}_c$  is the equivalent creep strain rate and  $\varepsilon_f^*$  is the multiaxial creep ductility which can be calculated using Eqn (12). By integrating Eqn (10), the total creep damage at any time can be calculated by

$$\omega = \int_0^t \frac{\dot{\varepsilon}_c}{\varepsilon_f^*} dt \quad (11)$$

The damage parameter  $\omega$  ranges from zero to unity with  $\omega = 0.0$  at time  $t = 0$  and failure occurring when  $\omega = 1.0$ . When the accumulated damage at the centroid of the element reaches unity, the element is considered fully creep damaged, thus progressive cracking is simulated ahead of the crack tip and the load carrying capacity is reduced to a value of close to zero. It must be noted that in this simulation approach, the crack is allowed to deviate from the initial crack plane and the effective crack extension is measured by taking the magnitude of crack growth ahead of the crack tip.

The multiaxial creep ductility,  $\varepsilon_f^*$ , in creep damage calculations can be estimated from the uniaxial creep ductility,  $\varepsilon_f$ , through a multiaxial strain factor (MSF) solution, such that

$$\varepsilon_f^* = \varepsilon_f MSF \quad (12)$$

The value of the MSF for a given material can be determined experimentally or through a failure mechanism model. There are many models [35]–[37] proposed to calculate the multiaxial strain factor. The one which has been used in this study is the Cocks and Ashby void growth model [35] using which the MSF can be calculated as

$$MSF = \sinh \left[ \frac{2}{3} \left( \frac{n-0.5}{n+0.5} \right) \right] / \sinh \left[ 2 \left( \frac{n-0.5}{n+0.5} \right) \frac{\sigma_m}{\sigma_e} \right] \quad (13)$$

where  $n$  is the power law creep exponent and  $\sigma_m/\sigma_e$  is the ratio between the mean (hydrostatic) and equivalent (von Mises) stress. This ratio is known as stress triaxiality.

### 3.2 NSW creep crack initiation model

The model developed by Nikbin, Smith and Webster (NSW) [2],[38] has been widely used to predict the steady state creep crack initiation and growth behaviour of metallic materials at high temperatures. The NSW prediction model is stress state dependent and, therefore, provides different prediction lines for plane stress and plane strain conditions. The model is based on a ductility exhaustion approach and the crack growth is considered to occur when a critical level of damage is attained at a characteristic

distance,  $r_c$ , ahead of the crack tip. Based on the NSW model, under steady state creep conditions the CCG rate,  $\dot{a}$ , can be predicted by

$$\dot{a}_{NSW} = \frac{(n+1)}{\varepsilon_f^*} (Ar_c)^{\frac{1}{(n+1)}} \left(\frac{C^*}{I_n}\right)^{\frac{n}{(n+1)}} \quad (14)$$

where  $\varepsilon_f^*$  is the multiaxial creep ductility and  $I_n$  is a non-dimensional function of  $n$ , values which are tabulated in [39]. It is recommended in [40] that  $\varepsilon_f^*$  in Eqn (14) is taken as the uniaxial creep ductility for plane stress conditions and reduced by a factor of 30 for plane strain conditions. The distance  $r_c$  in the NSW model is often taken as the material average grain size, thus is taken as 0.05mm in this study [11]. A modified version of the NSW model, known as NSW-MOD, has been derived in [41] to predict the CCG rate under steady state creep conditions by considering the dependency of creep strain on the crack tip angle,  $\theta$ , and the creep stress exponent,  $n$ , in addition to the stress state.

The lower and upper bounds for CCI time can be obtained using the steady state CCG rate,  $\dot{a}$ , and the CCG rate at the initial crack length,  $\dot{a}_0$ . The initial CCG rate can be estimated to be  $(n+1)$  times less than the steady state value [11]. Therefore, the CCI time may be described as

$$\frac{\Delta a}{\dot{a}} \leq t_i \leq \frac{(n+1)\Delta a}{\dot{a}} \quad (15)$$

Assuming steady state creep conditions ahead of the crack tip, the CCI time may be predicted using the NSW model by

$$\frac{\Delta a \varepsilon_f^*}{(n+1)(Ar_c)^{\frac{1}{(n+1)}}} \left(\frac{I_n}{C^*}\right)^{\frac{n}{(n+1)}} \leq t_i \leq \frac{\Delta a \varepsilon_f^*}{(Ar_c)^{\frac{1}{(n+1)}}} \left(\frac{I_n}{C^*}\right)^{\frac{n}{(n+1)}} \quad (16)$$

## 4 Creep crack initiation prediction results

FE simulations were performed on five specimen geometries (see Table 1 for the specimen details), under various load levels, as described in Tables 3-7. The predicted CCI results have been validated through comparison with experimental data presented in [11]. The number of test data sets available for each geometry are: 21 on C(T), one

on CS(T), three on DEN(T), five on M(T) and three on SEN(T). Additionally, for each of the specimen geometries examined, comparisons have been made between the predicted FE results and NSW prediction lines. For each FE simulation, the initiation time was recorded for a crack extension of 0.2mm and 0.5mm and  $t_{0.2}$  and  $t_{0.5}$  were predicted, respectively. Following the procedure explained in [7], the CCI times were verified when the first failure in any of the elements in the corresponding semi-circular ring was predicted. For each of the loading cases, the stress intensity factor at the initial crack length  $K(a_0)$  is evaluated using the solutions given in [14] and tabulated in Tables 3-7. Also included in these tables are the ratio of the initiation time at  $\Delta a = 0.5\text{mm}$ ,  $t_{0.5}$ , to the initiation time at  $\Delta a = 0.2\text{mm}$ ,  $t_{0.2}$ .

After completing the FE simulations, the predicted load line displacement rates,  $\dot{\Delta}$ , corresponding to  $t_{0.2}$  and  $t_{0.5}$  were determined using the seven-point incremental polynomial technique details of which can be found in ASTM E1457 standard [14]. Following the  $C^*$  validity criteria specified in [10], [14] it has been assumed that steady state creep conditions were established at the CCI times corresponding to 0.2mm and 0.5mm crack extensions. Therefore, the predicted CCI behaviour has been characterised using the crack tip fracture mechanics parameter  $C^*$ . It is known that 2D plane stress and plane strain simulations provide the upper and lower bound CCI trends, respectively [42]. In a previous CCG study by Mehmanparast [22] it was noted that 2D plane strain analysis using stress dependent creep ductility trends can encounter significant numerical difficulties. Therefore, plane stress FE simulations have been performed in the present study and the plane strain CCI trends are estimated by assuming the CCG rates to be five times higher than the predicted plane stress rates (see Eqn (6)), as suggested in [22]. Note that in the previous work by other researchers (see e.g. [3], [32], [33]), the predicted 2D plane strain CCG trends were found in good agreement with 3D prediction results, though plane strain simulations usually terminate due to numerical difficulties before any notable damage is predicted in the model.

#### **4.1 Mesh sensitivity analysis**

The mesh size effects on the predicted CCG results in FE simulations have been examined in [3], [4] and it has been shown that the CCG rates increase by decreasing the mesh size employed in the model. The mesh size effects are more pronounced in

CCI simulations using a semi-circular focused mesh structure. Therefore, a mesh sensitivity analysis has been conducted in this study to choose the optimum element size in CCI predictions. The mesh sensitivity analysis was performed by running 2D plane stress simulations on the CS(T) specimen geometry using the CS1 load case presented in Table 4. Simulations were repeated, under the same load level, by varying the focused mesh size around the crack tip region. Three cases of biased mesh size with the smallest element size, located at the crack tip, of  $10\mu\text{m}$ ,  $30\mu\text{m}$  and  $50\mu\text{m}$  were employed in the coarse, intermediate and fine mesh designs, respectively. The predicted creep crack initiation times corresponding to 0.2mm and 0.5mm crack extensions obtained from these analyses are shown in Fig. 6(a) and (b), respectively. It can be seen in Fig. 6 that reducing the mesh size leads to a decrease in the initiation time which, for the CS(T) specimen at CS1 loading condition, converges towards 20,000 and 37,600 hours for a crack extension of 0.2mm and 0.5mm, respectively. The mesh sensitivity analysis shows that the fine biased mesh design, with the element size ranging from  $10\mu\text{m}$  to  $500\mu\text{m}$  for a radial distance of 5mm from the crack tip, may be taken as the optimum mesh size below which the CCI prediction results would converge. The predicted creep damage around the crack tip region obtained from CCI simulations on the coarse, intermediate and fine mesh designs are presented in Fig. 7(a), (b) and (c), respectively. The results suggest that the element size has an effect on the damage initiation direction with the fine mesh showing an initiation angle,  $\theta_i$ , of around two times smaller than the coarse mesh.

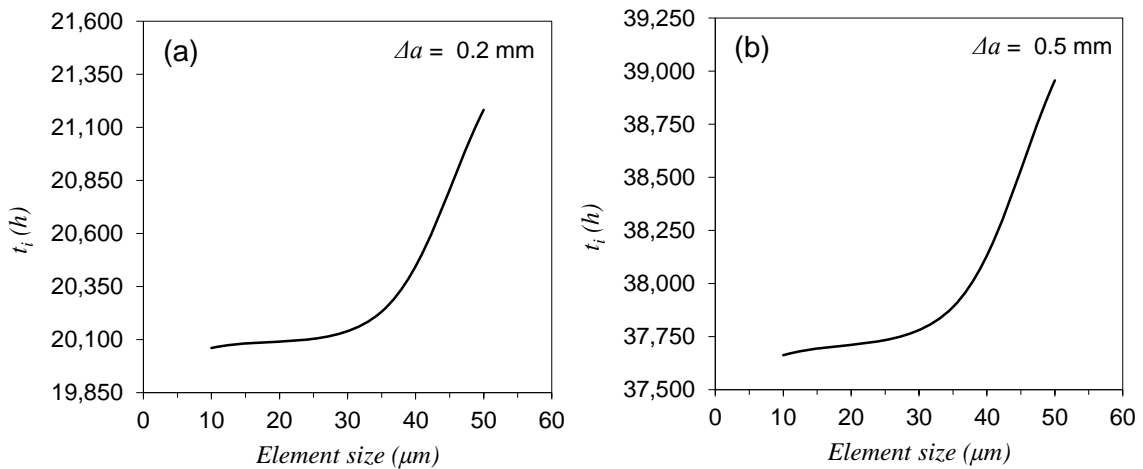


**Fig. 6.** Predicted creep crack initiation time against element size for CS(T) geometry for a crack extension of (a) 0.2mm, and (b) 0.5mm

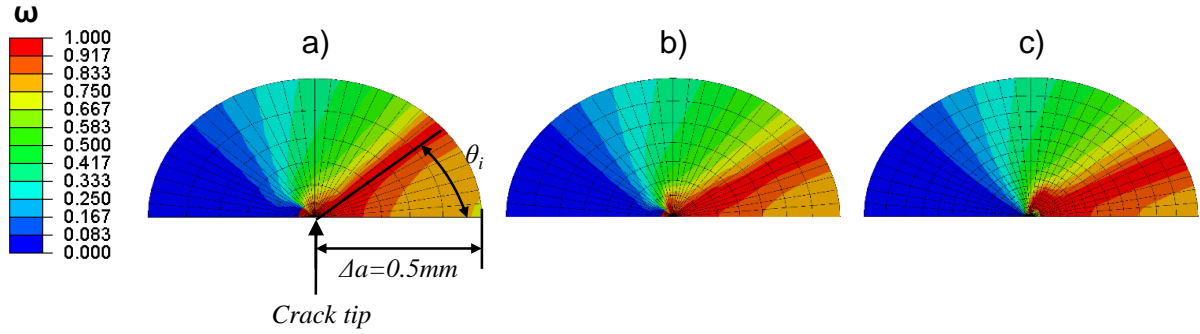


**Fig. 7.**  $t_{0.5}$  creep damage prediction ahead of the crack tip in different mesh size models (a, b and c) for CS(T) geometry

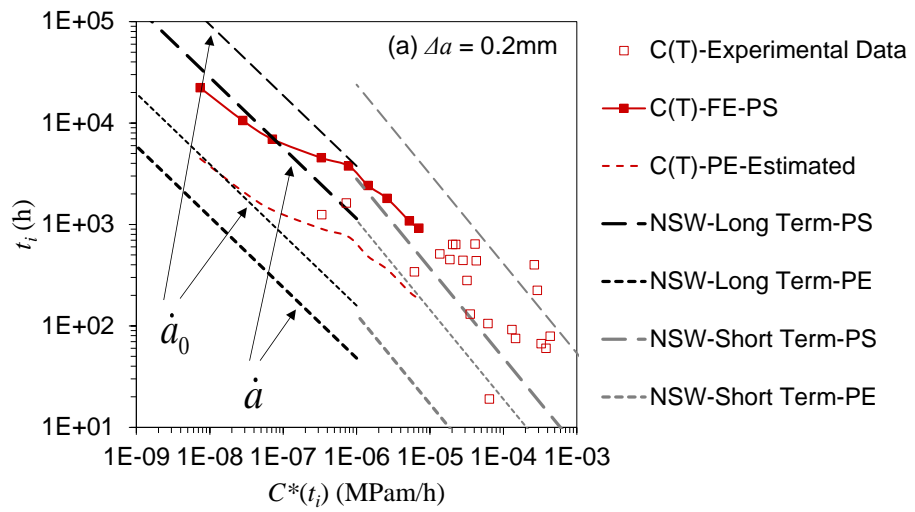
## 4.2 C(T) specimen geometry

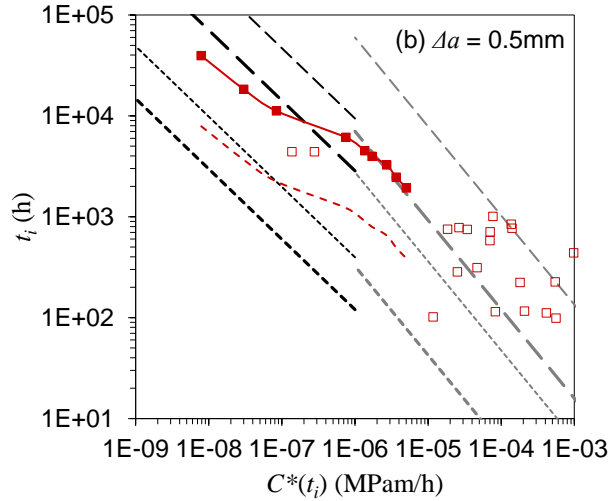
Nine loading cases have been examined on C(T) geometry and the loading conditions are given in Table 3. Also included in this table are the stress intensity factors at the initial crack length and normalised reference stress values for each of the loading cases considered. It can be seen in Table 3 that the normalised reference stress was less than unity for all the loading cases considered, indicating negligible plasticity in the simulations. The CCI prediction results are correlated with the  $C^*$  fracture mechanics parameter in Fig. 8(a) and (b) for 0.2mm and 0.5mm crack extensions, respectively. Also included in Fig. 8 is the estimated plane strain CCI trend, shown in dashed lines and identified by the notation PE, which has been estimated by shifting down the FE plane stress (PS) trend by a factor of five. Additionally, the plane stress and plane strain NSW prediction lines calculated based on the initial CCG rate,  $\dot{a}_0$ , and steady state CCG rate,  $\dot{a}$ , (see Eqn (16)) are shown in Fig. 8. For both PS and PE conditions, short-term and long-term NSW prediction lines are provided, which were calculated using constant creep ductility and average creep strain rate power law constants corresponding to the upper shelf and lower shelf regions (see Fig. 1 and Fig. 2). Finally, included in

Fig. 8 are the experimental data points using which the FE and NSW predictions can be validated.

**Table 3.** Loading cases applied on C(T) geometry

ID	$P$ (kN)	$K(a_0)$ (MPa $\sqrt{m}$ )	$\sigma_{ref}/\sigma_{0.2}$	$t_{0.5}/t_{0.2}$
CT1	2.50	4.32	0.13	1.77
CT2	3.75	6.48	0.20	1.73
CT3	5.00	8.64	0.26	1.61
CT4	7.50	12.96	0.40	1.35
CT5	10.00	17.28	0.53	1.20
CT6	12.25	21.17	0.65	1.64
CT7	14.50	25.05	0.77	1.81
CT8	15.75	27.21	0.83	2.28
CT9	17.00	29.37	0.90	2.10





**Fig. 8.** Comparison of predicted creep crack initiation trends with the experimental data and NSW predictions on C(T) geometry for a crack extension of (a) 0.2mm, and (b) 0.5mm

Fig. 8(a) and (b) show that three CCI trends are apparent in the FE PS predictions; a long-term trend at low  $C^*$  values, a short-term trend at high  $C^*$  values and a transition behaviour from short-term to long-term CCI behaviour at intermediate  $C^*$  values. It can be seen in Fig. 8 that the short-term (high  $C^*$ ) CCI trend predicted by FE PS simulations is greater than would follow from an extrapolation of the long-term (low  $C^*$ ) line. This indicates that if the short-term CCI trends are extrapolated to the very low  $C^*$  region, the  $t_{0.2}$  and  $t_{0.5}$  CCI times may be overestimated by around an order of magnitude. Further seen in Fig. 8(a) and (b) is that the long-term experimental data points fall in between the FE PS and estimated PE trends. If the short-term PS and PE trends are extrapolated to the higher  $C^*$  region, some of the existing short-term experimental data points on the C(T) specimen will fall between the FE PS and estimated PE trends, whereas other data points fall above the predicted PS trend. Comparison of the FE predictions and NSW lines in Fig. 8(a) and (b) shows that for both 0.2mm and 0.5mm crack extensions, the predicted FE PS trends fall close to the lower bound NSW lines (i.e. calculated using  $\dot{a}$ ) and the estimated PE trends fall upon or close to the upper bound NSW lines (i.e. calculated using  $\dot{a}_0$ ). Finally seen in Fig. 8(a) and (b) is that almost all experimental data points fall in between the short-term upper bound PS NSW line and the long-term upper bound PE NSW line.

### 4.3 CS(T) specimen geometry

A wider range of normalised reference stress has been examined on CS(T) geometry and the nine loading conditions are given in Table 4. It can be seen in this table that the normalised reference stress values for CS8 and CS9 loading cases were greater than unity, indicating considerable plasticity of the specimen under these loading conditions. The CCI predictions obtained from FE simulations and NSW lines are presented in Fig. 9(a) and (b) for the crack extension of 0.2mm and 0.5mm, respectively. Similar to C(T) specimen geometry, short-term, long-term and transition trends can be inferred in FE PS predictions. Given that there is only one set of experimental data on the CS(T) specimen, no experimental trends are seen; however the existing  $t_{0.2}$  data point falls between the FE PS and estimated PE trends, and the  $t_{0.5}$  data point coincides with the FE PS predicted trend. It can be seen in Fig. 9 that the long-term and short-term FE PS trends start to appear at  $C^*$  values of lower than  $1 \times 10^{-7}$  MPam/h and greater than  $1 \times 10^{-6}$  MPam/h, respectively. Also seen in this figure is that the FE PS and estimated PE trends fall upon or in between the lower bound (calculated using  $\dot{a}$ ) PS and PE NSW lines.

**Table 4.** Loading cases applied on CS(T) geometry

ID	$P$ (kN)	$K(a_0)$ (MPa $\sqrt{m}$ )	$\sigma_{ref}/\sigma_{0.2}$	$t_{0.5}/t_{0.2}$
CS1	2.50	4.19	0.17	1.88
CS2	3.75	6.29	0.26	1.69
CS3	5.00	8.39	0.35	1.60
CS4	7.50	12.58	0.52	1.39
CS5	10.00	16.77	0.70	1.26
CS6	12.50	20.97	0.87	1.35
CS7	14.00	23.48	0.98	1.99
CS8	15.50	26.00	1.08	2.48
CS9	16.00	26.84	1.12	2.20

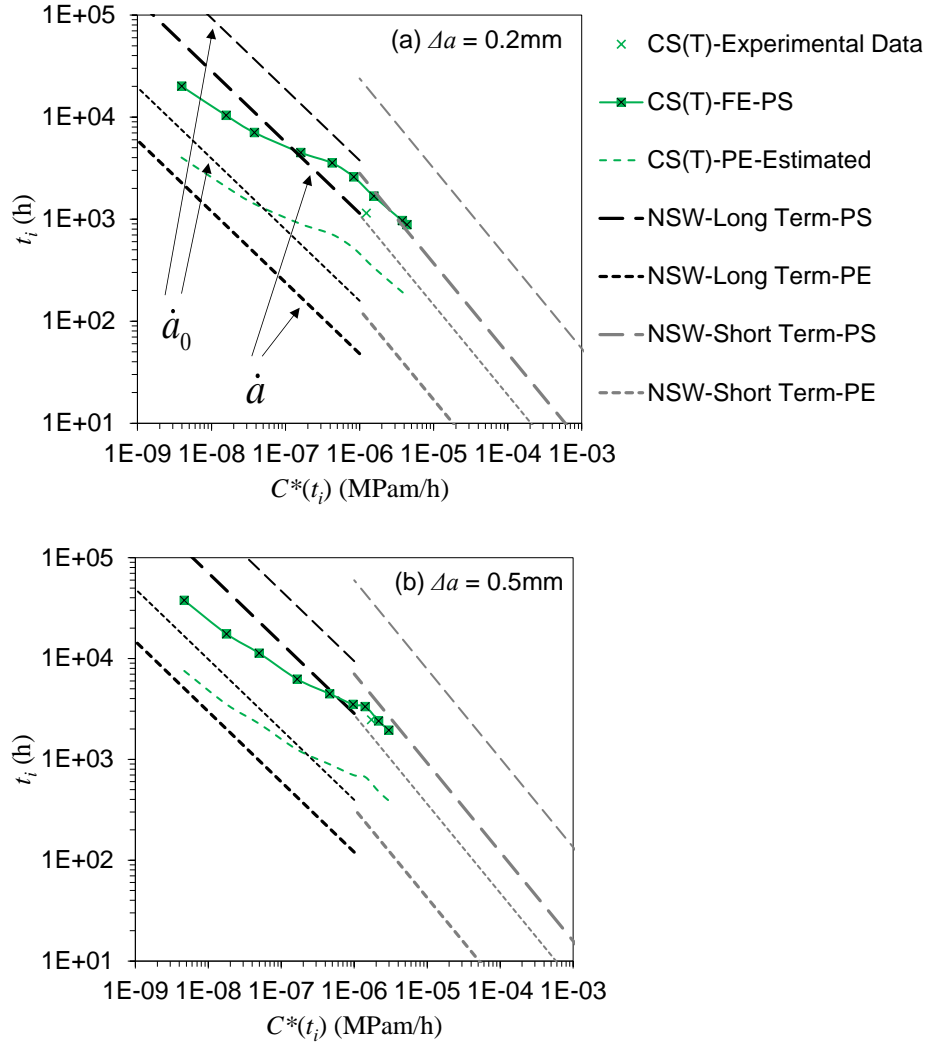


**Fig. 9.** Comparison of predicted creep crack initiation trends with the experimental data and NSW predictions on CS(T) geometry for a crack extension of (a) 0.2mm, and (b) 0.5mm

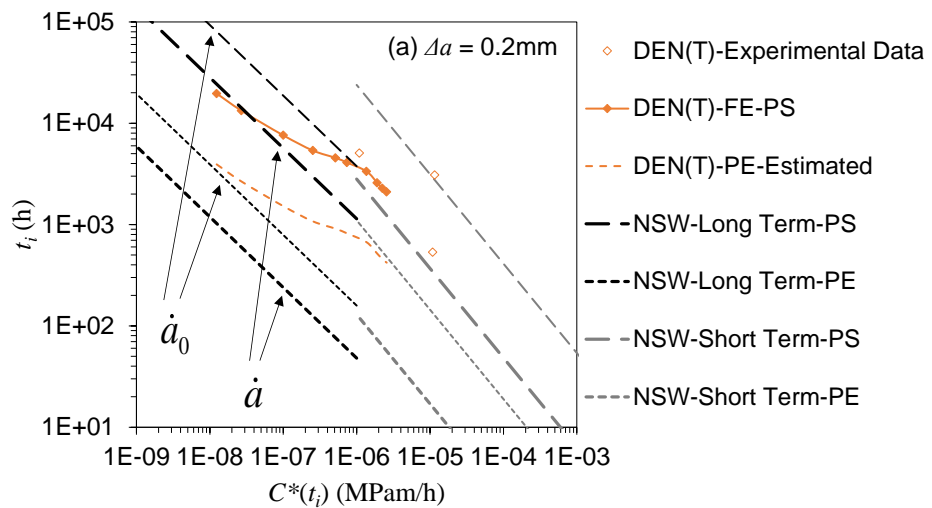
#### 4.4 DEN(T) specimen geometry

A summary of the loading conditions on the DEN(T) specimen is given in Table 5 where it can be seen that ten loading cases were examined. Due to numerical difficulties, higher load simulations were not possible and a smaller range of normalised reference stress was examined for this specimen geometry. The FE simulation results on this specimen geometry are presented and compared with the NSW prediction line and the existing experimental data in Fig. 10(a) and (b) for the crack extension of 0.2mm and 0.5mm, respectively. Similar to the previous two geometries, short-term, long-term and transition CCI trends were predicted by FE PS simulations. It can be seen in Fig. 10 that if the short-term FE PS trend is extrapolated to the higher  $C^*$  region, then one of

the existing experimental data points will fall close to the FE PS predictions, though the other two data points fall slightly above this predicted trend. Also observed in Fig. 10 is that the short-term and long-term upper bound (i.e. calculated using  $\dot{a}_0$ ) NSW PS prediction lines are in good agreement with the limited data points available on this specimen geometry; however, more experimental data in the high and low  $C^*$  regions are needed to confirm this observation.

**Table 5.** Loading cases applied on DEN(T) geometry

ID	$P$ (kN)	$K(a_0)$ (MPa $\sqrt{m}$ )	$\sigma_{ref}/\sigma_{0.2}$	$t_{0.5}/t_{0.2}$
DT1	4.50	1.75	0.10	1.82
DT2	5.63	2.19	0.13	1.74
DT3	8.50	3.31	0.20	1.52
DT4	11.25	4.38	0.26	1.50
DT5	13.50	5.25	0.31	1.46
DT6	15.50	6.03	0.36	1.39
DT7	18.50	7.20	0.43	1.36
DT8	20.50	7.97	0.48	1.61
DT9	21.50	8.36	0.50	1.43
DT10	22.25	8.65	0.52	1.18



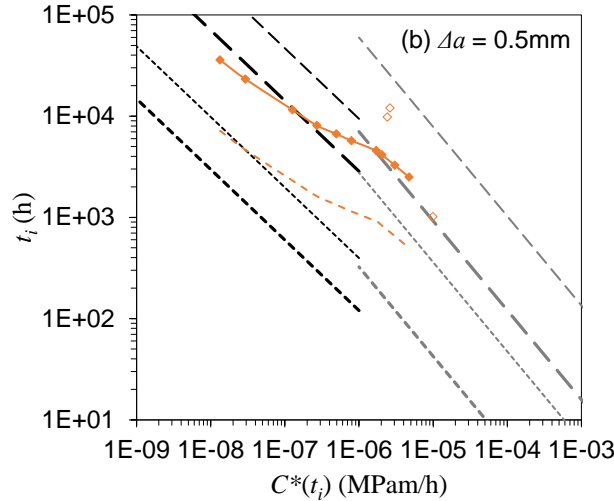


**Fig. 10.** Comparison of predicted creep crack initiation trends with the experimental data and NSW predictions on DEN(T) geometry for a crack extension of (a) 0.2mm, and (b) 0.5mm

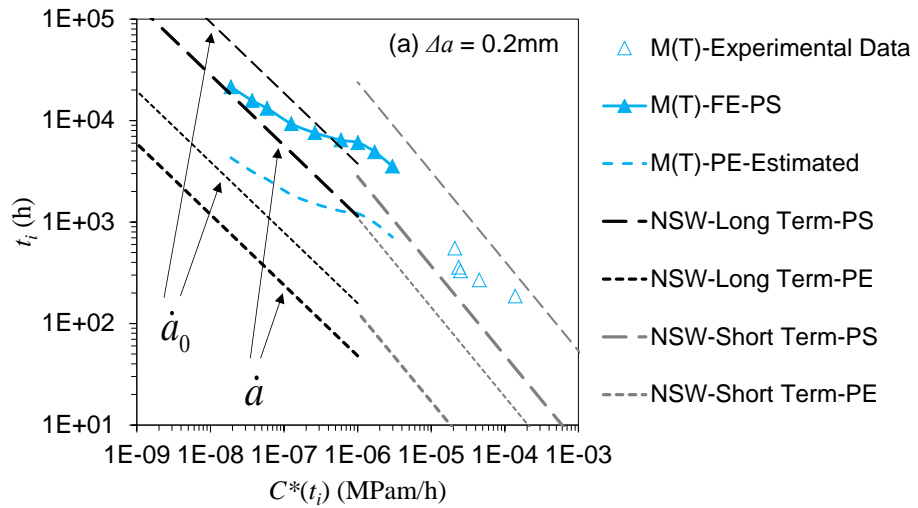
#### 4.5 M(T) specimen geometry

The details of the loading conditions applied on the M(T) geometry are given in Table 6 where, similar to the DEN(T) specimen geometry, a limited range of normalised reference stress is seen due to the numerical difficulties encountered with higher load simulations. The predicted CCI trends from FE simulations and NSW lines are presented in Fig. 11 and compared with the existing data on this specimen geometry. As seen in Fig. 11(a), the  $t_{0.2}$  CCI results obtained from FE PS simulations show long-term and short-term trends at  $C^*$  values of below  $1 \times 10^{-7}$  MPam/h and above  $1 \times 10^{-6}$  MPam/h, respectively, with a transition behaviour at intermediate  $C^*$  values. In the case of  $\Delta a = 0.5\text{mm}$ , the transition trend obtained from FE PS simulations appear at the intermediate  $C^*$  range of  $3 \times 10^{-7} < C^* < 2 \times 10^{-6}$  MPam/h. It can be seen in Fig. 11(a) and (b) that the experimental data points exist at the high  $C^*$  regions where there is no FE CCI result available. However, if the FE PS and estimated PE predicted trends are extrapolated to higher  $C^*$  region the majority of the existing data points will fall between these two trends. Note that although it appears in Fig. 11 that the FE results obtained from the highest load levels do not fall in the high  $C^*$  region, it is evident that the short-term CCI trends have just started to appear in the obtained FE results. Fig. 11(a) and (b) show that in the low  $C^*$  region there is an excellent agreement between the FE PS CCI trends and

the lower bound NSW PS line (calculated based on based on  $\dot{a}$ ). However, in the high  $C^*$  region the FE PS predictions fall in between the upper bound and lower bound NSW PS lines. Finally seen in Fig. 11(a) and (b) is that the existing experimental data points, which have been obtained from short-term high load tests, fall close to or in between the upper bound and lower bound NSW PS lines.

**Table 6.** Loading cases applied on M(T) geometry

ID	$P$ (kN)	$K(a_0)$ (MPa $\sqrt{m}$ )	$\sigma_{ref}/\sigma_{0.2}$	$t_{0.5}/t_{0.2}$
MT1	4.50	1.62	0.12	1.82
MT2	5.50	1.98	0.15	1.68
MT3	6.25	2.25	0.17	1.65
MT4	8.00	2.88	0.22	1.63
MT5	10.00	3.60	0.27	1.42
MT6	12.50	4.50	0.34	1.61
MT7	15.00	5.40	0.40	1.48
MT8	17.50	6.30	0.47	1.60
MT9	18.75	6.75	0.50	2.05



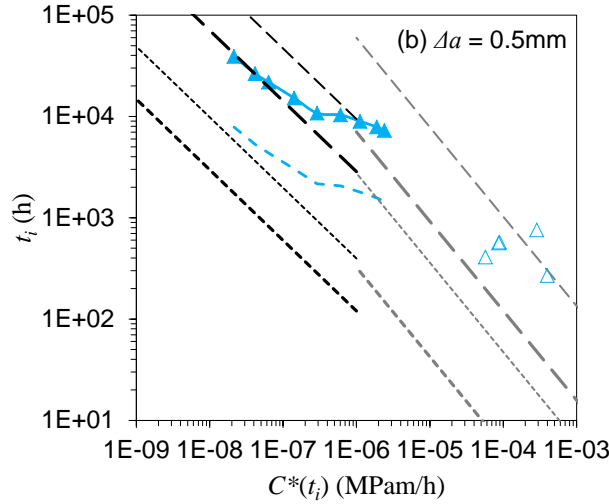


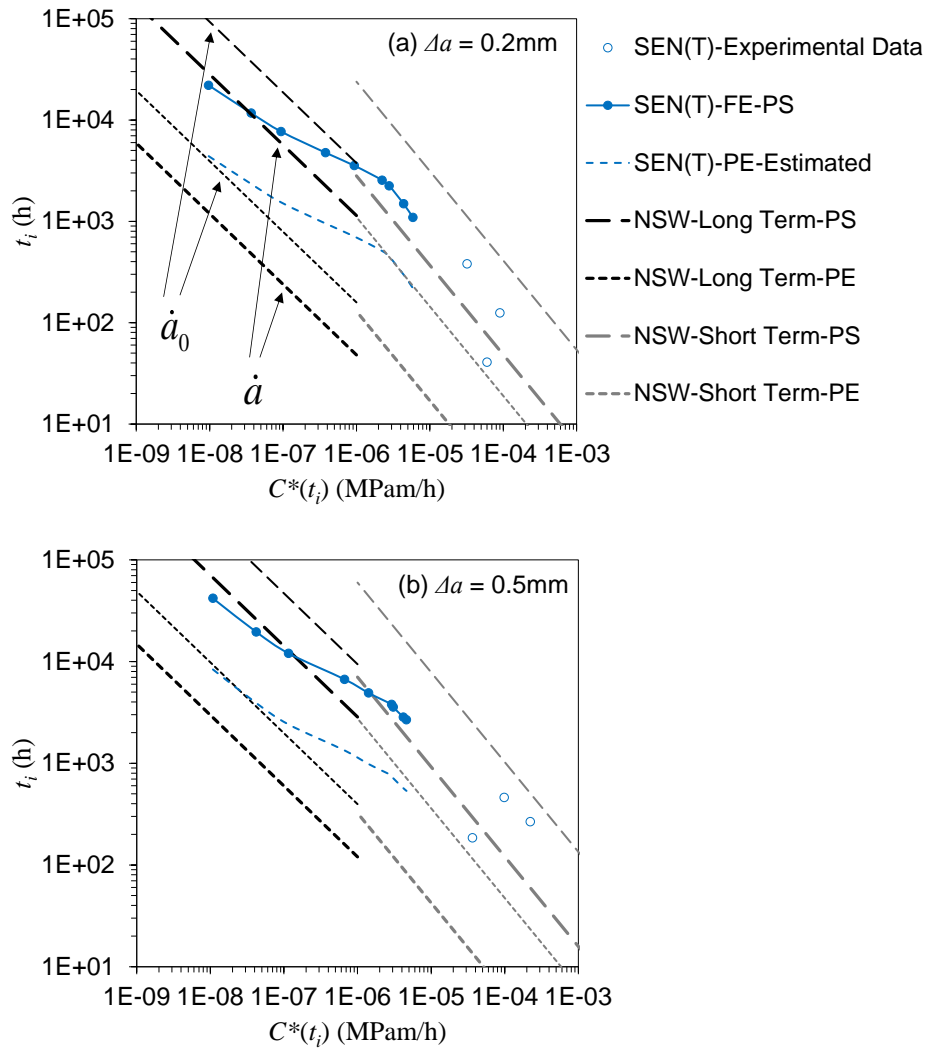
**Fig. 11.** Comparison of predicted creep crack initiation trends with the experimental data and NSW predictions on M(T) geometry for a crack extension of (a) 0.2mm, and (b)0.5mm

#### 4.6 SEN(T) specimen geometry

The loading conditions examined on the SEN(T) geometry have been summarised in Table 7. It can be seen in this table that the loading conditions result in a wider normalised reference stress range compared to those examined on DEN(T) and M(T) specimen geometries. Fig. 12 shows the predictions obtained from FE PS simulations along with the estimated shifted PE trends and the NSW prediction lines, which have been compared with the experimental data. Similarly to the other geometries, long-term and short-term CCI trends, with a transition region in between, have been predicted for  $t_{0.2}$  and  $t_{0.5}$ . For both  $\Delta a = 0.2\text{mm}$  and  $0.5\text{mm}$  crack extension criteria, the CCI transition region has been predicted to take place in the  $1 \times 10^{-7} < C^* < 2 \times 10^{-6}$  MPam/h region. As seen in Fig. 12 the limited short-term CCI data available on this specimen geometry fall upon or in between the FE PS and estimated PE trends if they are extrapolated to the higher  $C^*$  region. It can be observed in Fig. 12 that for 0.2mm and 0.5mm crack extension criteria, the long-term FE PS predictions are similar to those obtained from the lower bound NSW PS line (calculated based on  $\dot{a}$ ), whereas the short-term PS predictions fall between the upper bound and lower bound NSW PS lines. Furthermore, it is evident in Fig. 12 that the short-term and long-term CCI estimates for PE conditions coincide with the upper bound NSW PE lines (i.e. calculated using  $\dot{a}_0$ ).

**Table 7.** Loading cases applied on SEN(T) geometry

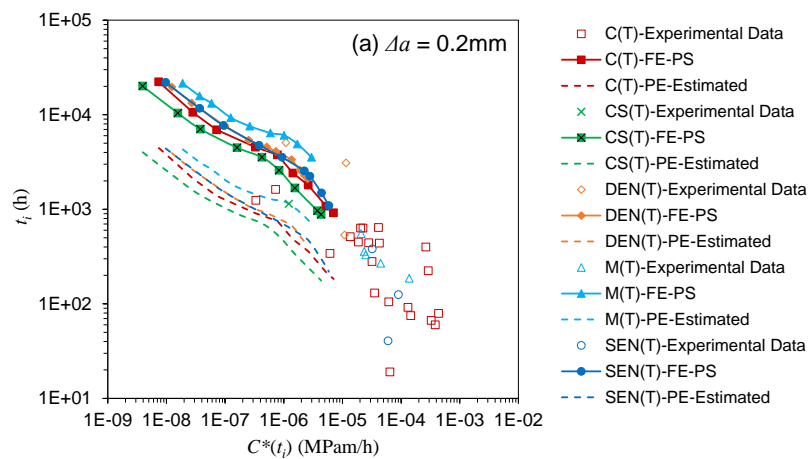
ID	$P$ (kN)	$K(a_0)$ (MPa $\sqrt{m}$ )	$\sigma_{ref}/\sigma_{0.2}$	$t_{0.5}/t_{0.2}$
ST1	4.38	4.25	0.16	1.90
ST2	6.50	6.31	0.23	1.67
ST3	8.75	8.49	0.31	1.56
ST4	13.25	12.86	0.47	1.40
ST5	17.50	16.99	0.62	1.38
ST6	22.50	21.84	0.80	1.49
ST7	23.75	23.05	0.84	1.59
ST8	25.00	24.27	0.89	1.91
ST9	26.00	25.24	0.92	2.45



**Fig. 12.** Comparison of predicted creep crack initiation trends with the experimental data and NSW predictions on SEN(T) geometry for a crack extension of (a) 0.2mm, and (b) 0.5mm

## 4.7 Comparison of CCI predictions for different geometries

The predicted CCI trends from the FE PS simulations for different specimen geometries presented in Fig. 8-12 are collated and compared in Fig. 13(a) and (b) for 0.2mm and 0.5mm crack extensions, respectively. Also included in Fig. 13 are the estimated PE trends and existing experimental data on all specimen geometries. It can be observed in Fig. 13(a) and (b) that the majority of experimental data points are available at the high  $C^*$  and within the experimental scatter no particular trend can be inferred for each of the specimen geometries examined. Note that the data scatter in  $t_{0.5}$ , particularly for C(T) specimen with the largest number of test data, is higher than  $t_{0.2}$ . The  $t_{0.2}$  and  $t_{0.5}$  FE prediction results show that similar CCI behaviour in the high, low and intermediate  $C^*$  regions can be observed in all specimen geometries. It can be observed that the trends at the low and high  $C^*$  regions are parallel to each other for all geometries, with the M(T) and CS(T) geometry showing the highest and the lowest CCI times, for a given values of  $C^*$ . Further seen in this figure is that the CCI trends from other three geometries are found to lie in between those of predicted for M(T) and CS(T), with coincident SEN(T) and DEN(T) trends falling closer to the M(T). This order of change in CCI times from high to low, starting with M(T) with the highest CCI time followed by DEN(T), SEN(T), C(T) and CS(T), is consistent in the high, low and intermediate  $C^*$  regions. Finally seen in Fig. 13(a) and (b) is that for the range of specimen geometries examined the transition from short-term to long-term CCI behaviour has been predicted to occur somewhat within the transition range of  $1 \times 10^{-7} < C^* < 2 \times 10^{-6}$  MPam/h.



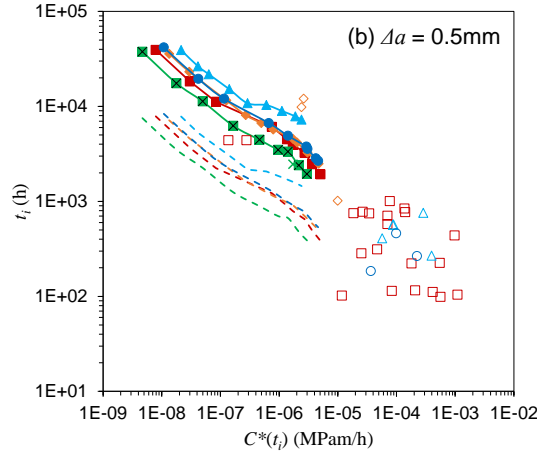


**Fig. 13.** Comparison of the predicted creep crack initiation trends on five specimen geometries

## 5 Discussion

The transition from short-term to long-term CCG behaviour has been experimentally observed in [6] and numerically predicted in [12], [22]. Although there are limited long-term CCI data points available for 316H at 550 °C, according to Eqn (6) where crack initiation time and CCG rate are correlated using the  $C^*$  parameter (assuming steady state creep conditions), a similar transition from short-term to long-term trends is also expected in the CCI behaviour of the material. The FE results have shown that by employing stress dependent creep properties in numerical simulations, the CCI behaviour of the material in the low (i.e. long-term), high (i.e. short-term) and intermediate  $C^*$  regions can be successfully predicted. The FE prediction results suggest that if the short-term CCI trends are extrapolated to the very low  $C^*$  region, the  $t_{0.2}$  and  $t_{0.5}$  CCI times may be overestimated by around an order of magnitude. Good agreements have been found between the FE CCI predictions and experimental results, where test data were available. The experimental data available in the literature for this material generally fall between the predicted FE PS and estimated PE estimated trends, for each of the specimen geometries examined. This suggests that the CCI behaviour of the material in the low and intermediate  $C^*$  regions, where there currently are few data points available, may be predicted by FE simulations. Furthermore, comparison of the experimental data with FE predictions shows that the approach to estimate the PE trends by shifting down the FE PS trends by a factor of five may be considered reasonable to predict the lower bound CCI behaviour of 316H stainless steel at 550 °C.

The  $t_{0.2}$  and  $t_{0.5}$  CCI trends for a range of fracture specimen geometries have been predicted in this study. In FE simulations on each of the specimen geometries, the loading cases were chosen in such a way that the corresponding stress intensity factors,  $K(a_0)$ , in 2D plane stress simulations are comparable to those applied on test specimens in [11]. The FE results have shown that a similar switch over from short-term to long-term CCI trend, with transition behaviour in between, has been observed in all five specimen geometries examined. For a given value of  $C^*$ , higher CCI trends are predicted for the low constraint (hence lower CCG rates and higher CCI times) M(T) specimen and the lowest CCI trend is predicted to occur in the CS(T) specimen, whilst the CCI trends from the other three geometries fall in between those predicted for M(T) and CS(T). The low constraint DEN(T) and SEN(T) geometries show coincident  $t_{0.2}$  and  $t_{0.5}$  CCI trends, whereas the high constraint C(T) specimen geometry shows slightly lower CCI trends compared to SEN(T) and DEN(T). The high and low CCI trends on M(T) and C(T), respectively, are consistent with the numerical investigation in [17] where it has been shown that the order of the crack tip constraint level from high to low is C(T), SEN(B), SEN(T) and M(T). Additionally, the results are also consistent with the CCG FE predictions obtained in [22], [32] and experimental studies in [11], [23]–[27], where the C(T) geometry showed the highest and M(T) the lowest CCG rates. Note that according to Eqn (6), higher CCG rates result in lower initiation time.

The numerical investigation in [17] did not include the CS(T) specimen, which according to [10] is also a high constraint specimen geometry. Additionally, due to the limited experimental data on CS(T) in [11], no experimental CCG trend could be inferred for this specimen geometry. However, FE CCG predictions on P92 steel in [43] showed that the CS(T) specimen geometry has a higher constraint compared to C(T), which is consistent with the lower CCI predictions obtained in this work. The coincident trends of DEN(T) and SEN(T) geometries can be explained by the fact that both geometries are considered as low constraint [10], furthermore, the CCG predictions in [43] showed that the CCG rates of SEN(T) are slightly lower than DEN(T), which explains why the CCI trends fall close to or upon each other.

The resulting ratio of the initiation time at 0.5mm to the initiation time at 0.2mm for all the geometries, listed in Tables 3-7 and presented in Fig. 14, indicates that the creep

ductility failure criterion and level of plasticity in a specimen can influence the  $t_{0.5}/t_{0.2}$  ratio. The predicted  $t_{0.5}/t_{0.2}$  values in Tables 3-7 and Fig. 14 show that in long-term (low load) simulations this ratio generally decreases as the load level (hence normalised reference stress) increases; however, when the corresponding  $C^*$  value falls upon the short-term CCI region, the  $t_{0.5}/t_{0.2}$  ratio starts to increase. Fig. 14 shows, for the range fracture specimen geometries examined, that the  $t_{0.5}/t_{0.2}$  ratio falls between 1.18 and 2.48 with the lowest and highest predicted ratios obtained at the intermediate and high normalised reference stress values.

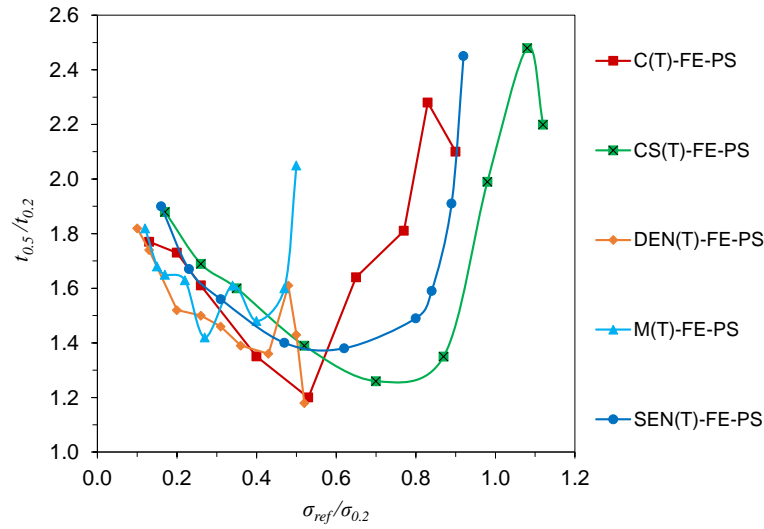


**Fig. 14.** Comparison of the predicted creep crack initiation trends on five specimen geometries

It can be seen in Fig. 8-Fig. 12 that for the range of specimen geometries examined, the predicted short-term and long-term  $t_{0.2}$  and  $t_{0.5}$  CCI trends obtained from FE PS simulations and PE estimates generally fall close to or in between the upper bound (i.e. calculated using  $\dot{a}_0$ ) and lower bound (i.e. calculated using  $\dot{a}$ ) PS and PE NSW lines, respectively. This indicates that when appropriate short-term and long-term uniaxial creep properties are employed in NSW models, the prediction results will be very similar to those obtained from FE simulations. Although NSW lines seem to provide acceptable CCI predictions for the high and low  $C^*$  regions, due to the dependency of this model on a constant creep ductility (see Eqn (14)), the NSW model fails to predict the transition from short-term to long-term CCI behaviour. However, by employing a stress dependent creep ductility model in FE simulations, the switch over from short-term to long-term CCI trend, which is expected to occur within the intermediate  $C^*$

range of between  $1 \times 10^{-7} < C^* < 2 \times 10^{-6}$  MPam/h, can be successfully predicted. It must be noted that NSW lines provide upper bound and lower bound CCG and CCI trends regardless of the specimen geometry on which the tests have been conducted. However, to account for the specimen constraint effects on the CCI behaviour of the material FE simulations need to be performed.

The focus of this work has been to investigate the influence of in-plane constraint effects on the CCI behaviour of 316H at 550 °C for a range of fracture mechanics specimen geometries, by employing a stress dependent uniaxial creep model in FE simulations. The influence of out-of-plane constraint effects on the creep crack initiation behaviour in each of the fracture mechanics specimens geometries considered in this work is currently being examined by the authors using 3D FE simulations and the results will be presented in future publications.

## 6 Conclusions

The creep crack initiation behaviour of Type 316H stainless steel at 550 °C has been predicted for a range of specimen geometries using stress dependent uniaxial creep properties implemented in FE simulations. The predicted creep crack initiation times have been correlated with the  $C^*$  fracture mechanics parameter. Short-term and long-term crack initiation trends with a transition region in between have been predicted for each of the specimen geometries considered. The creep crack initiation trends obtained from FE simulations have been found in good agreement with existing experimental data and NSW prediction lines. The FE results suggest that in addition to the stress state, which results in higher creep crack initiation times for plane stress conditions compared to the plane strain, the creep crack initiation behaviour of the material is sensitive to the specimen geometry and variations in the uniaxial creep properties from short-term to long-term tests. FE simulations have shown that the highest and lowest creep crack initiation trends were found in M(T) and CS(T) specimen geometry, respectively, with the predicted trends for other three geometries falling in between those of obtained from M(T) and CS(T). The FE simulation results have shown that for the range of specimen geometries and applied load level examined, the  $t_{0.5}/t_{0.2}$  ratio falls between 1.18 and 2.48 and is highly dependent on the applied stress (hence normalised

reference stress) level. Furthermore, the creep crack initiation transition behaviour from short-term to long-term trends has been predicted to occur within the range of  $1 \times 10^{-7} < C^* < 2 \times 10^{-6}$  MPam/h.



## REFERENCES

- [1] G. A. Webster and R. A. Ainsworth, *High temperature component life assessment*, 1st ed. London: Chapman & hall, 1994.
- [2] K. M. Nikbin, D. J. Smith, and G. A. Webster, "Prediction of Creep Crack Growth from Uniaxial Creep Data," *Proc. R. Soc. Lond. A. Math. Phys. Sci.*, vol. 396, no. 1810, pp. 183–197, Nov. 1984.
- [3] C.-S. Oh, N.-H. Kim, Y.-J. Kim, J.-H. Baek, Y.-P. Kim, and W.-S. Kim, "A finite element ductile failure simulation method using stress-modified fracture strain model," *Eng. Fract. Mech.*, vol. 78, no. 1, pp. 124–137, Jan. 2011.
- [4] M. Yatomi, K. M. Nikbin, and N. P. O'Dowd, "Creep crack growth prediction using a damage based approach," *Int. J. Press. Vessel. Pip.*, vol. 80, no. 7–8, pp. 573–583, Jul. 2003.
- [5] M. Yatomi, C. M. Davies, and K. M. Nikbin, "Creep crack growth simulations in 316H stainless steel," *Eng. Fract. Mech.*, vol. 75, no. 18, pp. 5140–5150, Dec. 2008.
- [6] D. W. Dean and D. N. Gladwin, "Creep crack growth behaviour of Type 316H steels and proposed modifications to standard testing and analysis methods," *Int. J. Press. Vessel. Pip.*, vol. 84, no. 6, pp. 378–395, Jun. 2007.
- [7] C. M. Davies, N. P. O'Dowd, K. M. Nikbin, and G. a. Webster, "An analytical and computational study of crack initiation under transient creep conditions," *Int. J. Solids Struct.*, vol. 44, no. 6, pp. 1823–1843, 2007.
- [8] C. M. Davies, "Predicting creep crack initiation in austenitic and ferritic steels using the creep toughness parameter and time-dependent failure assessment diagram," *Fatigue Fract. Eng. Mater. Struct.*, vol. 32, no. 10, pp. 820–836, 2009.
- [9] C. Davies, F. Mueller, K. Nikbin, N. O'Dowd, and G. Webster, "Analysis of Creep Crack Initiation and Growth in Different Geometries for 316H and Carbon Manganese Steels," *ASTM Int.*, vol. 3, no. 2, 2006.
- [10] "European Code of Practice for Creep Crack Initiation and Growth Testing of Industrially Relevant Specimens," in *Fatigue and Fracture Mechanics, Volume 35: (STP 1480)*, ASTM International, 2007.

- [11] C. M. Davies, D. W. Dean, M. Yatomi, and K. M. Nikbin, "The influence of test duration and geometry on the creep crack initiation and growth behaviour of 316H steel," *Mater. Sci. Eng. A*, vol. 510–511, pp. 202–206, 2009.
- [12] A. Mehmanparast, C. M. Davies, G. a. Webster, and K. M. Nikbin, "Creep crack growth rate predictions in 316H steel using stress dependent creep ductility," *Mater. High Temp.*, vol. 31, no. 1, pp. 84–94, 2014.
- [13] C. Davies and A. Mehmanparast, "Creep Crack Growth Modelling in 316H Stainless Steel," in *Advanced Materials Modelling for Structures SE - 11*, vol. 19, H. Altenbach and S. Kruch, Eds. Springer Berlin Heidelberg, 2013, pp. 109–120.
- [14] "ASTM E1457. Standard Test Method for Measurement of Creep Crack Growth Times in Metals," in *Annual Book of ASTM Standards*, ASTM International, 2007, pp. 1012–35, 2007.
- [15] T. Masaaki, K. Kiyoshi, and Y. Koichi, "Effect of specimen size on creep crack growth rate using ultra-large CT specimens for 1Cr-Mo-V steel," *Eng. Fract. Mech.*, vol. 40, no. 2, pp. 311–321, Jan. 1991.
- [16] P. Budden and R. Ainsworth, "The effect of constraint on creep fracture assessments," *Int. J. Fract.*, vol. 97, no. 1–4, pp. 237–247, 1999.
- [17] G. Z. Wang, B. K. Li, F. Z. Xuan, and S. T. Tu, "Numerical investigation on the creep crack-tip constraint induced by loading configuration of specimens," *Eng. Fract. Mech.*, vol. 79, pp. 353–362, Jan. 2012.
- [18] G. Z. Wang, X. L. Liu, F. Z. Xuan, and S. T. Tu, "Effect of constraint induced by crack depth on creep crack-tip stress field in CT specimens," *Int. J. Solids Struct.*, vol. 47, no. 1, pp. 51–57, Jan. 2010.
- [19] J. W. Zhang, G. Z. Wang, F. Z. Xuan, and S. T. Tu, "In-plane and out-of-plane constraint effects on creep crack growth rate in Cr–Mo–V steel for wide range of  $C^*$ ," *Mater. High Temp.*, vol. 32, no. 5, pp. 512–523, Sep. 2015.
- [20] J. W. Zhang, G. Z. Wang, F. Z. Xuan, and S. T. Tu, "Prediction of creep crack growth behavior in Cr–Mo–V steel specimens with different constraints for a wide range of  $C^*$ ," *Eng. Fract. Mech.*, vol. 132, pp. 70–84, Dec. 2014.

- [21] J. W. Zhang, G. Z. Wang, F. Z. Xuan, and S. T. Tu, “The influence of stress-regime dependent creep model and ductility in the prediction of creep crack growth rate in Cr – Mo – V steel,” *Mater. High Temp.*, vol. 65, pp. 644–651, 2015.
- [22] A. Mehmanparast, “Prediction of creep crack growth behaviour in 316H stainless steel for a range of specimen geometries,” *Int. J. Press. Vessel. Pip.*, vol. 120–121, pp. 55–65, Aug. 2014.
- [23] P. Budden and D. Dean, “Constraint effects on creep crack growth,” in *Proceedings of the Creep Eighth International Conference on Creep and Fatigue at Elevated Temperatures*, 2007.
- [24] A. Bettinson, N. O’Dowd, K. Nikbin, and G. Webster, “Experimental investigation of constraint effects on creep crack growth,” *ASME 2002 Press. Vessel. Pip. Conf.*, no. American Society of Mechanical Engineers, p. 143e50, 2002.
- [25] B. Ozmat, A. S. Argon, and D. M. Parks, “Growth modes of cracks in creeping type 304 stainless steel,” *Mech. Mater.*, vol. 11, no. 1, pp. 1–17, Mar. 1991.
- [26] Y. Takahashi, T. Igari, F. Kawashima, S. Date, N. Titoh, and Y. Noguchi, “High temperature crack growth behavior of high-chromium steels,” *SMiRT*, p. 1904e15, 2005.
- [27] C. M. Davies, R. C. Wimpory, D. W. Dean, and B. Way, “Specimen geometry effects on creep crack initiation and growth in parent materials and weldments,” *Proc. ASME 2011 Press. Vessel. Pip. Div. Conf.*, 2011.
- [28] F. Norton, *The creep of steel at high temperatures*. New York: McGraw-Hill, 1929.
- [29] T. Anderson, *Fracture mechanics: fundamentals and application*. Boston: CRC Press, 1991.
- [30] A. Mehmanparast, C. M. Davies, D. W. Dean, and K. M. Nikbin, “The influence of pre-compression on the creep deformation and failure behaviour of Type 316H stainless steel,” *Eng. Fract. Mech.*, vol. 110, pp. 52–67, 2013.
- [31] Simulia Corp, *Abaqus 6.14 Analysis User’s Guide*, Providence, RI, Published by

- Dassault Systemes Simulia Corp, 2014.
- [32] N.-H. Kim, C.-S. Oh, Y.-J. Kim, C. M. Davies, K. Nikbin, and D. W. Dean, “Creep failure simulations of 316H at 550°C: Part II – Effects of specimen geometry and loading mode,” *Eng. Fract. Mech.*, vol. 105, pp. 169–181, Jun. 2013.
- [33] C.-S. Oh, N.-H. Kim, Y.-J. Kim, C. Davies, K. Nikbin, and D. Dean, “Creep failure simulations of 316H at 550°C: Part I – A method and validation,” *Eng. Fract. Mech.*, vol. 78, no. 17, pp. 2966–2977, Dec. 2011.
- [34] M. Yatomi and M. Tabuchi, “Issues relating to numerical modelling of creep crack growth,” *Eng. Fract. Mech.*, vol. 77, no. 15, pp. 3043–3052, Oct. 2010.
- [35] A. C. F. Cocks and M. F. Ashby, “Creep fracture by coupled power-law creep and diffusion under multiaxial stress,” *Met. Sci.*, vol. 16, no. 10, pp. 465–474, Oct. 1982.
- [36] M. W. Spindler, “The multiaxial creep ductility of austenitic stainless steels,” *Fatigue Fract. Eng. Mater. Struct.*, vol. 27, no. 4, pp. 273–281, Apr. 2004.
- [37] J. R. Rice and D. M. Tracey, “On the ductile enlargement of voids in triaxial stress fields\*,” *J. Mech. Phys. Solids*, vol. 17, no. 3, pp. 201–217, Jun. 1969.
- [38] K. M. Nikbin, D. J. Smith, and G. A. Webster, “An Engineering Approach to the Prediction of Creep Crack Growth,” *J. Eng. Mater. Technol.*, vol. 108, no. 2, pp. 186–191, Apr. 1986.
- [39] C. F. Shih, *Tables of Hutchinson-Rice-Rosengren singular field quantities*. MRL E-Providence, Ri: Brown University Technical Report, 1983.
- [40] M. Tan, N. J. . Celard, K. . Nikbin, and G. . Webster, “Comparison of creep crack initiation and growth in four steels tested in HIDA,” *Int. J. Press. Vessel. Pip.*, vol. 78, no. 2001, pp. 737–747, 2001.
- [41] M. Yatomi, N. P. O’Dowd, K. M. Nikbin, and G. A. Webster, “Theoretical and numerical modelling of creep crack growth in a carbon–manganese steel,” *Eng. Fract. Mech.*, vol. 73, no. 9, pp. 1158–1175, Jun. 2006.
- [42] P. J. Sun, G. Z. Wang, F. Z. Xuan, S. T. Tu, and Z. D. Wang, “Three-dimensional numerical analysis of out-of-plane creep crack-tip constraint in compact tension

- specimens,” *Int. J. Press. Vessel. Pip.*, vol. 96–97, pp. 78–89, Aug. 2012.
- [43] L. Zhao, L. Xu, Y. Han, and H. Jing, “Quantifying the constraint effect induced by specimen geometry on creep crack growth behavior in P92 steel,” *Int. J. Mech. Sci.*, vol. 94–95, pp. 63–74, May 2015.